Ba_2YIrO_6: A cubic double perovskite material with Ir^{5+} ions

T. Dey,[1,*] A. Maljuk,[1] D. V. Efremov,[1] O. Kataeva,[1,2,3] S. Gass,[1] C. G. F. Blum,[1] F. Steckel,[1] D. Gruner,[1] T. Ritschel,[1] A. U. B. Wolter,[1] J. Geck,[1] C. Hess,[1,4] K. Koepernik,[1] J. van den Brink,[1,5] S. Wurmehl,[1,5] and B. Büchner[1,4,5]

[1]*Leibniz Institute for Solid State and Materials Research IFW, Institute for Solid State Research, 01069 Dresden, Germany*

[2]*Kazan Federal University, Kremlevskaya Strasse 18, 420008, Kazan, Russia*

[3]*A.E. Arbuzov Institute of Organic and Physical Chemistry, Russian Academy of Sciences, Arbuzov Strasse 8, Kazan 420088, Russia*

[4]*Center for Transport and Devices of Emergent Materials, TU Dresden, 01069 Dresden, Germany*

[5]*Institute for Solid State Physics, Technische Universität Dresden, D-01062 Dresden, Germany*

(Received 2 October 2015; published 22 January 2016)

Materials with a $5d^4$ electronic configuration are generally considered to have a nonmagnetic ground state ($J = 0$). Interestingly, Sr_2YIrO_6 (Ir^{5+} having $5d^4$ electronic configuration) was recently reported to exhibit long-range magnetic order at low temperature and the distorted IrO_6 octahedra were discussed to cause the magnetism in this material. Hence, a comparison of structurally distorted Sr_2YIrO_6 with cubic Ba_2YIrO_6 may shed light on the source of magnetism in such Ir^{5+} materials with $5d^4$ configuration. Besides, Ir^{5+} materials having $5d^4$ are also interesting in the context of recently predicted excitonic types of magnetism. Here we report a single-crystal-based analysis of the structural, magnetic, and thermodynamic properties of Ba_2YIrO_6. We observe that in Ba_2YIrO_6 for temperatures down to 0.4 K, long-range magnetic order is absent but at the same time correlated magnetic moments are present. We show that these moments are absent in fully relativistic *ab initio* band-structure calculations; hence, their origin is presently unclear.

DOI: 10.1103/PhysRevB.93.014434

I. INTRODUCTION

The iridates have become an interesting playground for material researchers as they show novel ground states due to competing interactions between the crystal field (CF), the Coulomb interaction (U), and the spin-orbit coupling (SOC) [1]. To name a few examples, $(Sr/Ba)_2IrO_4$ [2–6], $Sr_3Ir_2O_7$ [7–9], and $(Na/Li)_2IrO_3$ [10–15] have been studied intensively in recent times, both experimentally and theoretically.

In all the above-mentioned compounds, the iridium ion is magnetic with a formal oxidation state +4 ($5d^5$). In contrast, materials with a $4d^4$ or $5d^4$ electronic configuration (such as Re^{3+}, Ru^{4+}, Os^{4+}, Ir^{5+}) are believed to be in a Van Vleck–type nonmagnetic band insulating ground state with a completely filled $J = 3/2$ manifold having a total angular momentum $J = 0$ [16]. Such a nonmagnetic ground state is realized in $NaIrO_3$ [17,18].

However, recently two independent theoretical studies proposed that the interplay between U and SOC in some of these materials may lead to novel magnetism governed by gapped singlet-triplet excitations [19,20], although the ground states obtained in these two studies are different. Meetei *et al.* [20] proposed a magnetic phase diagram for the d^4 Mott insulators which consists of a nonmagnetic ($J = 0$) and two different ferromagnetic phases ($J = 2$ and $J = 1$). The authors have identified the double perovskite materials as good candidates to observe such novel magnetic states.

Recently, in the double perovskite material Sr_2YIrO_6 with Ir^{5+} ions, a transition to an antiferromagnetic long-range order was observed below 1.3 K [21]. Cao *et al.* [21] assigned the structural distortion of Sr_2YIrO_6 originating in the monoclinic structure (space group $P2_1/n$) with highly distorted IrO_6 octahedra as the driving force for the long-range magnetic order in this compound. Hence, the motivation to study the Ba analog Ba_2YIrO_6 is twofold: (i) the investigation of other Ir^{5+} materials in general to verify or discard the theoretically predicted excitonic magnetism in the Van Vleck–type d^4 Mott insulators [19,20], and (ii) the investigation of cubic analogs with Ir^{5+} to shed light on the impact of noncubic symmetry on the magnetism in such systems.

The crystal structure of Ba_2YIrO_6 has been described using a cubic symmetry (space group $Fm\bar{3}m$) [22–24] as well as a monoclinic symmetry (space group $P2_1/n$) with $\beta = 90.039^\circ$ (Ref. [25]). The monoclinic description with $\beta \sim 90^\circ$ closely matches with the cubic description. In any case, since all previous studies are based on polycrystalline samples, it is important to revisit the crystal structure of Ba_2YIrO_6 using single crystals and in particular shedding light on the magnetic properties of this material.

In this work, we report the growth of Ba_2YIrO_6 single crystals and the details of their structural, magnetic, thermal, and electrical transport properties. Ba_2YIrO_6 clearly crystallizes in a cubic double perovskite-type (space group $Fm\bar{3}m$) structure, as demonstrated by our single-crystal and powder (on crushed single crystals) x-ray diffraction study, and, hence, is a suitable material to address the open issues in Ir^{5+} materials as outlined above. The crystals are semiconducting and show a paramagnetic behavior in the temperature range 0.43–300 K. Our susceptibility and heat capacity measurements show no sign of long-range magnetic ordering down to at least 0.4 K. The effective magnetic moment ($\mu_{\text{eff}} = 0.44\ \mu_B/\text{Ir}$) obtained from the Curie-Weiss fit of our susceptibility data is unexpected for the anticipated $J = 0$ material. This could be arising from chemical disorder in the crystals. We performed *ab initio* calculations in the LDA+U scheme to gain insight into the ground state. The results show that the initially metallic band becomes insulating

*Present address: Experimental Physics VI, EKM, University of Augsburg, 86159 Augsburg, Germany; tusdey@gmail.com

due to the interplay of the spin-orbit and the Coulomb interaction.

II. EXPERIMENTAL DETAILS

Single crystals of Ba_2YIrO_6 were grown using high-purity starting materials $BaCO_3$ (Alpha Aesar 99.997%), IrO_2 (Alpha Aesar 99.99%), and Y_2O_3 (Alpha Aesar 99.999%). Ultra-dry $BaCl_2$ (Alpha Aesar 99.5%) was used as flux. The stoichiometric mixture of the starting materials and the flux were put inside a platinum crucible covered with a platinum lid to reduce flux evaporation. The mixture was heated to 1250–1300 °C, held at this temperature for 24 h, and then slowly cooled to 950 °C. After that it was cooled to room temperature very fast by switching off the furnace. Cubic-size single crystals (typical dimensions $0.3 \times 0.3 \times 0.3$ mm^3, also compare Fig. 1) were precipitated at the bottom of the platinum crucible. After dissolving the flux in water, the single crystals were collected and used for further characterization.

Single-crystal x-ray diffraction (XRD) data of Ba_2YIrO_6 were collected on a Bruker AXS Kappa APEX diffractometer with graphite-monochromated Mo $K\alpha$ radiation ($\lambda = 0.710\,73$ Å) using the complete sphere mode at 198(2) K. The following programs were used to collect and analyze the data: the data collection was done with APEX2 [26], the data reduction with SAINT [27], the numerical absorption correction was applied using SADABS [28], the structure solution was obtained with SHELXS-97 [29], and the structure refinement was performed by full-matrix least-squares against F^2 using SHELXL-97 [29]. CSD 427064 contains the supplementary crystallographic data for this work. Room temperature powder XRD patterns were obtained using a Stoe Stadi-P diffractometer with Mo $K\alpha_1$ radiation equipped with a curved Ge(111) primary monochromator and a Dectris Mythen 1 K detector. Our data were analyzed with the Rietveld method using the FULLPROF program [30]. The homogeneity and the chemical composition of the crystals were analyzed using energy-dispersive x-ray (EDX) analysis with a scanning electron microscope (SEM Philips XL 30).

Magnetization measurements were performed as a function of temperature (T) and magnetic field (H) on randomly oriented single crystals of a total mass ~57 mg in a Quantum Design MPMS in the temperature range 0.43–300 K using the *iHelium3* option below 1.8 K. Heat capacity measurements (C_P) were performed on 10–12 crystals (mass ~2 mg) in the temperature range 0.4–10 K using the ^{3}He option of a Quantum Design PPMS. The resistivity was measured as a function of temperature in the range 4.2–300 K in a homemade device. The contacts on the sample were made using graphite epoxy in the four-point contact geometry.

III. RESULTS AND DISCUSSION

A. Microstructure analysis

Figure 1 exemplarily shows an as-grown Ba_2YIrO_6 single crystal (left panel). The middle panel of Fig. 1 shows the SEM image of a single crystal in backscattered electron (BSE) mode. Our SEM analysis suggests that the composition is homogeneous over the crystals. However, we cannot exclude the possibility of a certain amount of off-stoichiometry, e.g., $Ba_2Y_{1+d}Ir_{1-d}O_{6-d}$.

B. XRD and crystal structure

Single-crystal XRD measurements (shown in the right panel of Fig. 1) performed on several pieces from different preparation batches showed a high quality of the crystals, proven by the good internal consistency of the data collected using the full-sphere mode and an extremely low R factor (less than 1%). These measurements confirm that Ba_2YIrO_6 crystallizes in a cubic double perovskite structure with space group $Fm\bar{3}m$ (No. 225), similar to results as reported in Refs. [22–24] based on XRD measurements on polycrystalline samples. The results of the structural refinement of the single-crystal XRD measurements at 198(2) K are summarized in Table I. The atomic positions and thermal parameters are listed in Table II.

Furthermore, we have measured powder XRD on crushed single crystals. The resulting XRD pattern is shown in Fig. 2. Traces of unreacted Y_2O_3 (~2%) are found in the XRD pattern with the main peak corresponding to Y_2O_3 marked by an arrow along with small amounts of Pt from the crucible that are contaminating the surfaces of the crystal. All the major peaks in the powder XRD pattern are indexed with space group $Fm\bar{3}m$ as shown in Fig. 2. The double-phase Rietveld refinement of the powder XRD pattern (shown in Fig. 2) using space group $Fm\bar{3}m$ for Ba_2YIrO_6 and $Ia\bar{3}$ for Y_2O_3 results in refinement parameters $R_p = 2.54$ and $R_{wp} = 3.88$. The lattice constants obtained from single-crystal XRD and powder XRD on crushed crystals are consistent with earlier reports [22–25]. We find no signature of any structural transition of the crystals from room temperature (powder XRD) down to 198(2) K

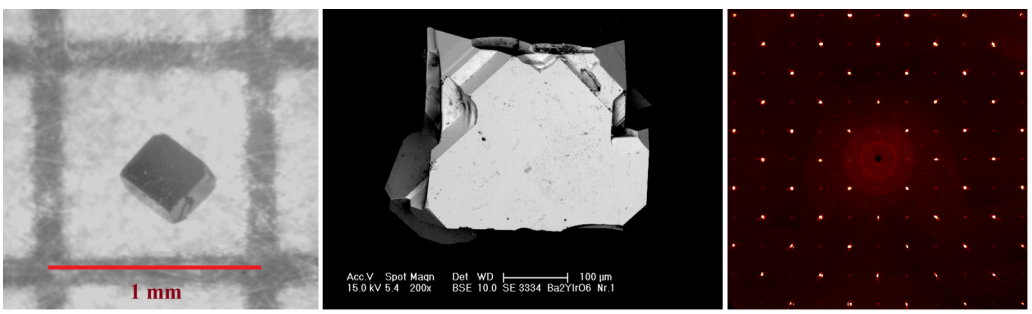

FIG. 1. (Left) Optical image of a Ba_2YIrO_6 single crystal placed on a millimeter graph paper. (Middle) SEM image of one Ba_2YIrO_6 single crystal in backscattering electron (BSE) mode. (Right) A representative single-crystal XRD pattern in the (h0l) plane at 198(2)K.

TABLE I. Crystal data for Ba_2YIrO_6 from single-crystal diffractometry.

Temperature (K)	198(2)
Crystal (for XRD) size (mm^3)	$0.15 \times 0.16 \times 0.19$
Space group	$Fm\bar{3}m$ (No. 225)
a (Å)	8.3387(8)
V (Å^3)	579.8(2)
Z	4
ρ_{calc}(g cm^{-3})	7.467
μ (mm^{-1})	46.149
Multiscan absorption correction	$0.041 \leqslant T \leqslant 0.055$
θ range (°)	0.95 – 45.1
Collected reflections	12012
Independent reflections	$162(R_{int} = 0.0486)$
Observed reflections	$162[I \geqslant 2\sigma(I)]$
Refined parameters	8
R	0.0096
wR^2	$0.0270[I > 2\sigma(I)]$
Max residual electron density (e Å^{-3})	1.459
Min residual electron density (e Å^{-3})	−0.559
Goodness of fit	1.350

(single-crystal XRD). Also, no anomaly is seen in our magnetic susceptibility and heat capacity measurement (discussed later), which suggests the absence of any structural transition down to 0.4 K.

The crystal structure of Ba_2YIrO_6 based on our refinement results is shown in Fig. 3. An alternating arrangement of IrO_6 (pink) and YO_6 (light blue) octahedra, with the Ba atoms (yellow) placed in between, form the crystal structure. Please note that the Ir^{5+} ions in this structure build up a face-centered cubic (fcc) network. Attempts to allow site disorder in the refinement were not leading to better fit results; hence, we concluded that site disorder does not play a role here. This is consistent with the ionic size of Y^{3+} and Ir^{5+} ions being very different, rendering site disorder rather unlikely. The same arguments hold for off-stoichiometry. The distortion of IrO_6 octahedra as present in the monoclinic Sr_2YIrO_6 is absent in the cubic Ba_2YIrO_6.

C. Resistivity

Figure 4 shows the semiconductor-type resistivity of a Ba_2YIrO_6 single crystal as a function of temperature. The measurement was done at a constant current of $I = 5$ μA. The resistivity at room temperature is $\rho(300\ \text{K}) = 40\ \text{m}\Omega\,\text{cm}$ and increases exponentially with decreasing temperature. At

TABLE II. Atomic positions and thermal parameters for a Ba_2YIrO_6 single crystal at 198(2) K.

Atoms	Site	x	y	z	Site occ.	U_{iso}
Ba(1)	8c	0.25	0.25	0.25	1	1.0675
Y(1)	4a	0	0	0	1	0.75887
Ir(1)	4b	0.5	0.5	0.5	1	0.81458
O(1)	24e	0.25944(2)	0	0	1	0.51547

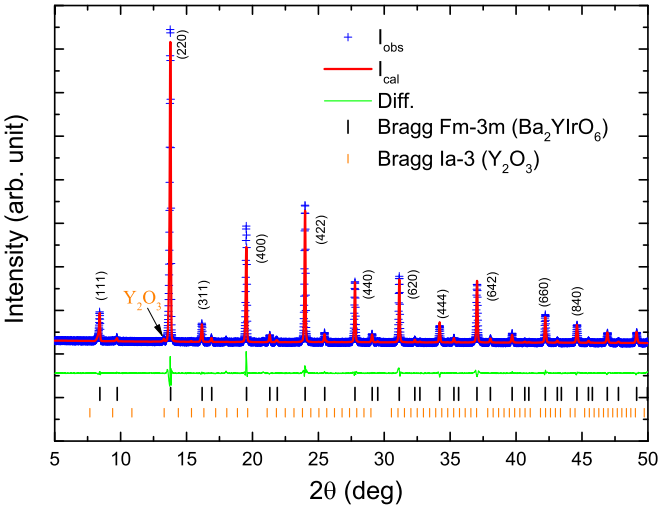

FIG. 2. Powder XRD pattern (blue cross) and its double-phase refinement (red solid line); space groups $Fm\bar{3}m$ for Ba_2YIrO_6 and $Ia\bar{3}$ for Y_2O_3 are shown. The Bragg positions corresponding to space groups $Fm\bar{3}m$ and $Ia\bar{3}$ are shown as black and orange vertical lines, respectively. The green line shows the difference between the observed and the calculated patterns. The main reflection corresponding to Y_2O_3 is marked with an arrow.

temperatures lower than ∼170 K, the resistivity increases to very high values, hindering a correct measurement with our device. The inset of Fig. 4 shows the Arrhenius plot of the resistivity data. From room temperature down to 160 K, $\ln(\rho)$ is inversely proportional to the temperature, i.e., $\rho \propto \exp(\triangle/2k_BT)$. Our analysis yields an energy gap of $\triangle \approx 221$ meV. It should be noted that the geometrical error of the contacts is quite high due to the small sample size. This may influence the accuracy of the absolute value of the resistivity; however, the overall temperature dependence and therefore the energy gap is unaffected.

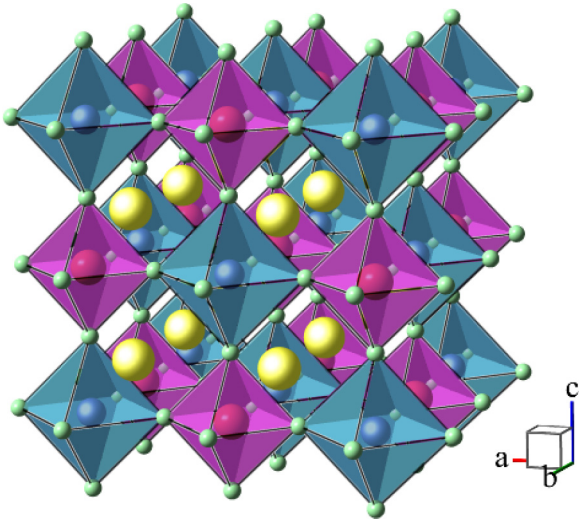

FIG. 3. Crystal structure of Ba_2YIrO_6. The yellow and the green atoms represent Ba and O, respectively. The pink and light blue octahedra correspond to the IrO_6 and YO_6 octahedra, respectively.

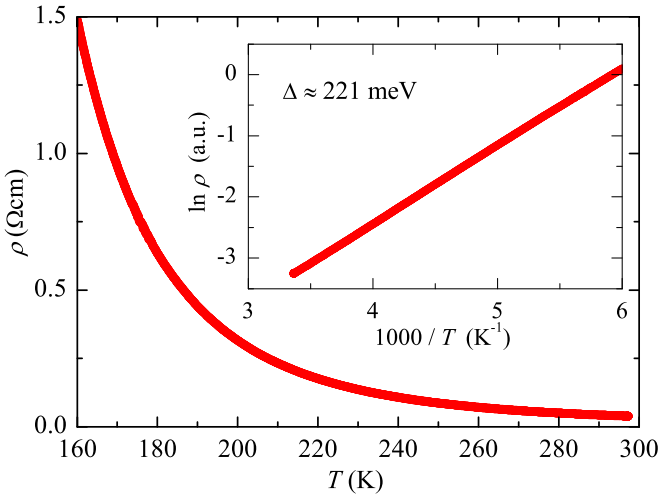

FIG. 4. Resistivity (ρ) as a function of temperature for a single-crystal piece of Ba_2YIrO_6. (Inset) Arrhenius plot of the resistivity.

D. Magnetization

Since the magnetization of the material is expected to be small, we have taken special care to increase the sample mass and to subtract the background signal of the sample holder. Figure 5 shows the zero-field-cooled susceptibility data as a function of temperature in an external magnetic field of 5 kOe for our as-grown single crystals. No signature of any long-range magnetic order is found in the measured temperature range 0.43 K $\leqslant T \leqslant$ 300 K. Moreover, no splitting between zero-field-cooled (ZFC) and field-cooled (FC) susceptibilities are observed between 1.8 and 300 K, even when measured in small applied fields of 50 Oe [31]. The susceptibility data is fitted with a Curie-Weiss (CW) law $\chi(T) = \chi_0 + C/(T-\theta)$ in the temperature range 15–300 K (shown in Fig. 5). This fitting gives a temperature-independent susceptibility contribution $\chi_0 = 5.83 \times 10^{-4}$ cm^3/mol, a Curie constant $C = 0.024\,7$ cm^3 K/mol (effective magnetic moment $\mu_{\text{eff}} =$ 0.44 μ_B/Ir), and a Weiss temperature $\theta \sim -8.9$ K. The inverse susceptibility (after subtracting χ_0) is plotted on the right axis of the figure. Below ~15 K, deviations from the CW fitting occur, which probably stem from even larger antiferromagnetic spin correlations in the low-temperature regime, or from a small temperature-dependent contribution to the Van Vleck susceptibility, which has not been taken into account in the fit but which has been observed, e.g., for Eu^{3+} [32].

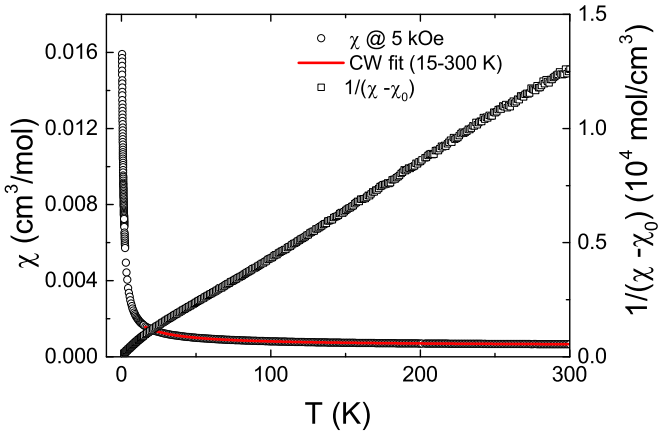

FIG. 5. (Left axis) Magnetic susceptibility in an external magnetic field $H = 0.5$ kOe of as-grown crystals as a function of temperature along with its fit according to Curie-Weiss (CW) law in the range 15–300 K. (Right axis) The inverse susceptibility (after subtracting χ_0 obtained from the CW fit).

Since materials with $5d^4$ electronic configuration are expected to be Van Vleck–type nonmagnetic, it is interesting to extract the Van Vleck part in the susceptibility for this material. For insulating materials one can consider $\chi_0 = \chi_{\text{core}} + \chi_{vv}$, where χ_{core} is the core diamagnetic susceptibility and χ_{vv} is Van Vleck paramagnetic susceptibility. In case of Ba_2YIrO_6, $\chi_{\text{core}} = -1.68 \times 10^{-4}$ cm^3 K/mol (obtained by adding the core diamagnetic susceptibility for individual ions [33]), which results in $\chi_{vv} = 7.51 \times 10^{-4}$ cm^3 K/mol. This value is of the same order of magnitude as for other Ir^{5+} ($5d^4$) materials (see Table III).

The effective magnetic moment ($\mu_{\text{eff}} = 0.44\ \mu_B$/Ir) is unusual for an expected $J = 0$ material. The simplest explanation for the magnetic response could be the presence of a few percent of Ir^{4+} ions (which are known to be magnetic) caused by oxygen deficiency. To verify or discard the presence of oxygen vacancies, we have annealed the as-grown crystals under 700 bar oxygen pressure at 500 °C for 2 days. Magnetization measurements on these oxygen-annealed crystals yield identical results compared with those of the as-grown crystals. This probably suggests that there are no oxygen vacancies in the as-grown crystals.

Another possibility for the presence of Ir^{4+} ions is a partial substitution of Y^{3+} by Ir^{4+} ions, as it was seen in the cubic double perovskite material $Ba_2(Y_{0.67}Ir_{0.33})IrO_6$ with the formal oxidation state of Ir +4.5 [34]. The small Curie constant of Ba_2YIrO_6 and Weiss temperature could result from the presence of a few percent of Ir^{4+} ions (~5% of $J = 1/2$ spins). A third scenario accounts for Ir^{6+} ions created due to the intermixing and/or off-stoichiometry. For double perovskite materials with Ir^{6+} ions, μ_{eff} is reported to be more than 3 μ_B/Ir [35]. Hence, the presence of a small amount of Ir^{6+} ions can result in the observed $\mu_{\text{eff}} = 0.44\ \mu_B$/Ir.

To understand the origin of the magnetic moments, we further analyzed the isothermal magnetization data $M(H)$ at 480 mK as shown in Fig. 6. We were able to fit our data with a modified Brillouin function $M(H) = \chi_0 H + f N_A g \mu_B J B_J(g\mu_B J H/k_B T)$, where f, N_A, g, and k_B represent a scaling factor to account for a finite number of paramagnetic impurities, the Avogadro constant, the Landé g factor, and the Boltzmann constant, respectively (see Fig. 6). The first linear term $\chi_0 H$ describes the core plus the Van Vleck contributions (see above), while the second term, the Brillouin function B_J, represents the behavior of paramagnetic spins as a function of a magnetic field at a particular temperature.

Our analysis suggests the presence of ~ 2% of $J = 1/2$ spins in the material and a g factor of 2.14. This result matches quite well with the estimate from the CW fitting assuming $g = 2.14$. We also tried to vary the J value according to the different scenarios outlined above, but the fitting result depicted in Fig. 6 is very robust. However, the fitted g value is decreasing from 2.14 to 1.2 for $J = 1/2$ to $J = 3/2$, respectively.

TABLE III. A comparison of the Van Vleck susceptibility (χ_{vv}), effective magnetic moment (μ_{eff}), and Curie-Weiss temperature (θ_{CW}) of different $5d^4$ materials.

Material	Electronic config.	χ_{vv} (cm^3 K/mol)	μ_{eff}	θ_{CW}	Reference
Ba_2YIrO_6	$5d^4$	7.51×10^{-4}	$0.44\mu_B$/Ir	-8.9 K	This work
Sr_2YIrO_6	$5d^4$	10.11×10^{-4}	$0.91\mu_B$/Ir	-229 K	[21]
$NaIrO_3$	$5d^4$	19×10^{-4}	$0.28\mu_B$/Ir	-2.2 K	[17]

While the temperature-independent susceptibility contribution from the CW fitting yields $\chi_0 = 5.83 \times 10^{-4}$ cm^3/mol, we obtain a larger value of $\chi_0 = 15.0 \times 10^{-4}$ cm^3/mol from the field dependence of the magnetization. This mismatch probably arises from non-negligible antiferromagnetic spin correlations in Ba_2YIrO_6 which have not been taken into account in the Brillouin function. Further detailed investigations are planned in order to shed light on the nature of the magnetic correlations in Ba_2YIrO_6, which seem to increase at low temperatures.

E. Heat capacity

The low-temperature specific heat (C_P) data for zero field is shown on the left axis of Fig. 7. Our specific heat data is qualitatively similar to that of Sr_2YIrO_6 [21]. We do not find any signature of magnetic ordering down to 0.4 K in Ba_2YIrO_6, and no anomaly is resolved even in the $\frac{dC_P}{dT}$ vs T plot, which is shown on the right axis of Fig. 7, in contrast to what has been reported for Sr_2YIrO_6.

F. Ground state in DFT theory

To understand the origin of the insulating ground state in Ba_2YIrO_6 we performed density functional theory (DFT) calculations of the electronic structure. Our calculations were carried out within the local (spin) density approximation [L(S)DA] using the Full Potential Local Orbital band-structure package (FPLO) [36,37]. A k mesh of $12 \times 12 \times 12$ k points in the whole Brillouin zone was employed. To take correlation effects in the Ir $5d$ shell into account we adopted the L(S)DA+U scheme. Due to the rather sizable spin-orbit interaction of the Ir atoms, the full relativistic four-component Dirac scheme was used.

Similar to other iridates, the LDA results suggest a metallic state for Ba_2YIrO_6 as indicated by a finite density of states (DOS) at the Fermi level E_F [Fig. 8(a)]. The Ir $5d$ and O $2p$ states have strong hybridization due to strong metal-ligand covalency. The Ir $5d$ electrons give a contribution to the total density of states in three energy windows: from -6.5 eV to -4.5 eV, from -1 eV to 0.5 eV, and from 2.5 eV to 4.5 eV. From Fig. 8 one can see that the t_{2g} and e_g states are well separated. The spin-orbit interaction [Fig. 8(b)] considerably changes the bands near the Fermi level, but still the DOS at the Fermi level remains finite. Analyzing the partial density of states, one can identify a splitting of the $5d$ states into single-particle $5d_{3/2}$ and $5d_{5/2}$ contributions. To obtain an insulating ground state one needs to take into account strong correlations in the mean-field approximation (LDA+U). We introduce a Hubbard $U \approx 1.4$ eV and Hunds $J = 0.5$ eV for the Ir $5d$ shell. These values of U and J give a magnetic solution for the system with the magnetic moment of the order of $2\mu_B$ in the absence of the spin-orbit interaction. But with the spin-orbit interaction the magnetic solution becomes unstable and instead we find, at a configuration with an effective single particle, $J_z = S_z = 0$, as one can see from Figs. 8(c) and 9. The presence of a moderate U opens a gap $\Delta = 0.2$ eV, pushing up one of the bands of predominantly $5d_{5/2}$ character. This value for the gap is close to one that we have found experimentally from the resistivity measurements. From this we conclude that the insulating state has a similar origin as in other iridates: the interplay of spin-orbit interaction and correlations.

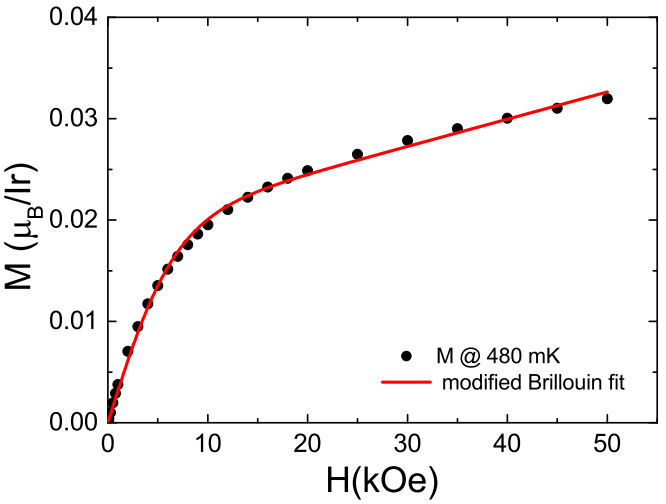

FIG. 6. The isothermal magnetization curve for as-grown crystals at $T = 480$ mK together with a fit according to a modified Brillouin function; for details see text.

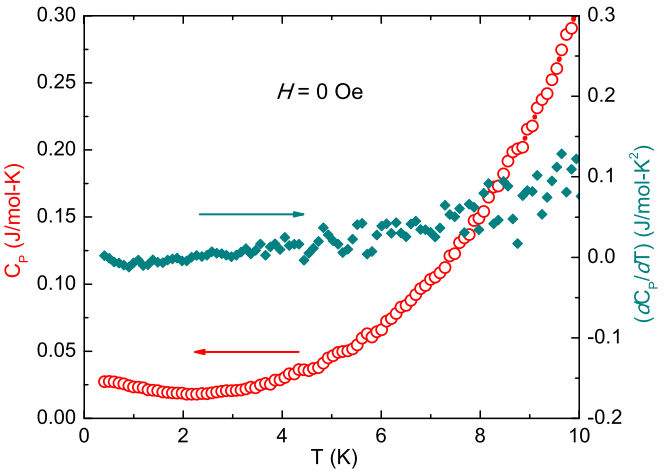

FIG. 7. (Left axis) The specific heat (C_P) of several Ba_2YIrO_6 single crystals in zero field as a function of temperature (T). (Right axis) The derivative of C_P.

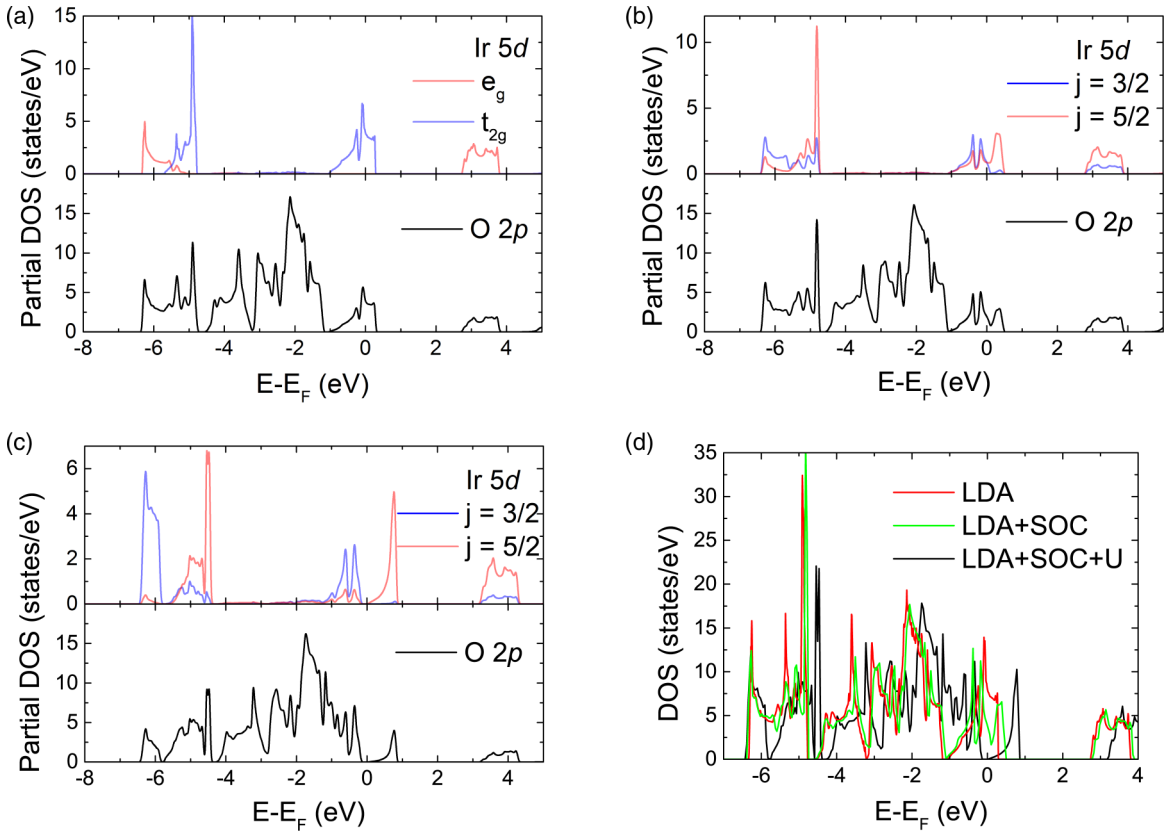

FIG. 8. Partial density of states (pDOS) for Ir and O atoms: (a) LDA scheme, (b) LDA+SOC scheme, (c) LDA+SOC+U scheme, (d) total density of states, calculated in the frame of LDA, LDA+SOC, LDA+SOC+U.

IV. CONCLUSIONS

Single crystals of the double perovskite Ba_2YIrO_6 were grown by the flux method. Our XRD measurements on single and crushed crystals unambiguously reveal that this material crystallizes in a cubic double perovskite structure. In contrast to the general expectation, we found that Ba_2YIrO_6 is paramagnetic from our bulk susceptibility measurements. The susceptibility data is fitted well with the CW formula and results in an effective magnetic moment $\mu_{\text{eff}} = 0.44\ \mu_B/\text{Ir}$ and a Weiss temperature $\theta_{\text{CW}} = -8.9$ K. However, it is not clear at the moment if this is the manifestation of proposed gapped excitonic magnetism [19,20] in d^4 materials or caused by chemical disorder and/or off-stoichiometry (the presence of Ir^{4+} or Ir^{6+} ions). Density-functional-based electronic structure calculations show that in the LDA+U approach a magnetic ground state is stable for physical values of the Hubbard U and Hund's rule exchange J, but only if relativistic effects are treated on a scalar relativistic level (no spin-orbit coupling). In fully relativistic calculations we find that the spin-orbit coupling drives the system into a Mott insulator with a value of the gap close to the experimental value. However, at the same time the system becomes nonmagnetic. This calls for further investigations of the origin of the unexpected magnetism in this material and suggests that the origin of the observed magnetic moments is related to electronic many-body effects, the theoretical description of which likely stretches beyond the reach of effective mean-field approaches such as LDA+U.

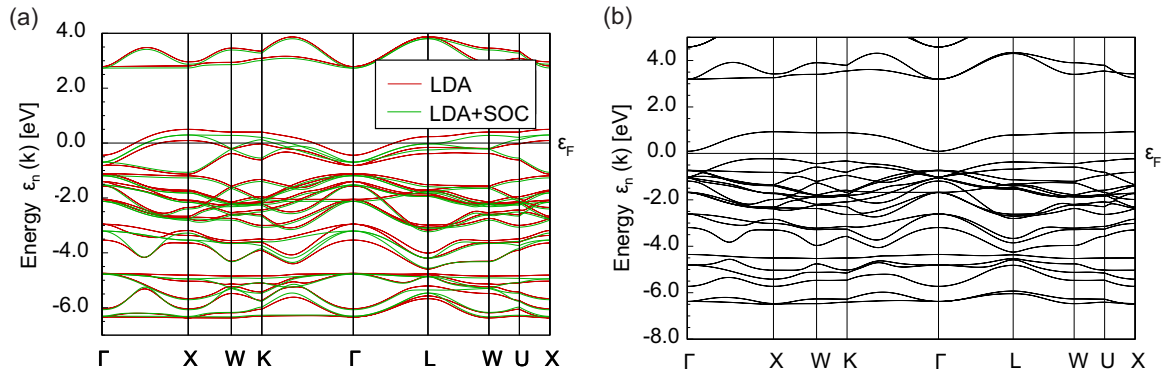

FIG. 9. Band structure: (a) LDA and LDA+SOC and (b) LDA+SOC+U.

ACKNOWLEDGMENTS

We would like to thank F. Hammerath, D. Khomskii, and T. Saha Dasgupta for fruitful discussion; S. Müller-Litvyani and J. Werner for technical support; and L. Giebeler for support with the XRD data. S.W. acknowledges funding by the Deutsche Forschungsgemeinschaft DFG under the Emmy-Noether Programme (Project No. WU595/3-1) and by a Materials World Network grant (Project No. WU595/5-1). O.K. acknowledges DFG support (Project No. KN 393/20-1). This work has been supported by DFG in SFB 1143.

[1] For a review, see *Frontiers of 4d- and 5d-Transition Metal Oxides*, edited by G. Cao and L. DeLong (World Scientific, Singapore, 2013).

[2] B. J. Kim, H. Jin, S. J. Moon, J.-Y. Kim, B.-G. Park, C. S. Leem, J. Yu, T. W. Noh, C. Kim, S.-J. Oh, J.-H. Park, V. Durairaj, G. Cao, and E. Rotenberg, Phys. Rev. Lett. **101**, 076402 (2008).

[3] B. J. Kim, H. Ohsumi, T. Komesu, S. Sakai, T. Morita, H. Takagi, and T. Arima, Science **323**, 1329 (2009).

[4] V. M. Katukuri, H. Stoll, J. van den Brink, and L. Hozoi, Phys. Rev. B **85**, 220402(R) (2012).

[5] H. Okabe, M. Isobe, E. Takayama-Muromachi, A. Koda, S. Takeshita, M. Hiraishi, M. Miyazaki, R. Kadono, Y. Miyake, and J. Akimitsu, Phys. Rev. B **83**, 155118 (2011).

[6] S. Boseggia, R. Springell, H. C. Walker, H. M. Ronnow, Ch. Ruegg, H. Okabe, M. Isobe, R. S. Perry, S. P. Collins, and D. F. McMorrow, Phys. Rev. Lett. **110**, 117207 (2013).

[7] S. Fujiyama, K. Ohashi, H. Ohsumi, K. Sugimoto, T. Takayama, T. Komesu, M. Takata, T. Arima, and H. Takagi, Phys. Rev. B **86**, 174414 (2012).

[8] G. Cao, Y. Xin, C. S. Alexander, J. E. Crow, P. Schlottmann, M. K. Crawford, R. L. Harlow, and W. Marshall, Phys. Rev. B **66**, 214412 (2002).

[9] J.-M. Carter and H.-Y. Kee, Phys. Rev. B **87**, 014433 (2013).

[10] Y. Singh, S. Manni, J. Reuther, T. Berlijn, R. Thomale, W. Ku, S. Trebst, and P. Gegenwart, Phys. Rev. Lett. **108**, 127203 (2012).

[11] Y. Singh and P. Gegenwart, Phys. Rev. B **82**, 064412 (2010).

[12] S. Manni, S. Choi, I. I. Mazin, R. Coldea, M. Altmeyer, H. O. Jeschke, R. Valentí, and P. Gegenwart, Phys. Rev. B **89**, 245113 (2014).

[13] J. Chaloupka, G. Jackeli, and G. Khaliullin, Phys. Rev. Lett. **105**, 027204 (2010).

[14] C. C. Price and N. B. Perkins, Phys. Rev. Lett. **109**, 187201 (2012).

[15] H. Gretarsson, J. P. Clancy, X. Liu, J. P. Hill, E. Bozin, Y. Singh, S. Manni, P. Gegenwart, J. Kim, A. H. Said, D. Casa, T. Gog, M. H. Upton, H.-S. Kim, J. Yu, V. M. Katukuri, L. Hozoi, J. van den Brink, and Y.-J. Kim, Phys. Rev. Lett. **110**, 076402 (2013).

[16] G. Chen and L. Balents, Phys. Rev. B **84**, 094420 (2011).

[17] M. Bremholm, S. E. Dutton, P. W. Stephens, and R. J. Cava, J. Solid State Chem. **184**, 601 (2011).

[18] L. Du, X. Sheng, H. Weng, and X. Dai, Europhys. Lett. **101**, 27003 (2013).

[19] G. Khaliullin, Phys. Rev. Lett. **111**, 197201 (2013).

[20] O. N. Meetei, W. S. Cole, M. Randeria, and N. Trivedi, Phys. Rev. B **91**, 054412 (2015).

[21] G. Cao, T. F. Qi, L. Li, J. Terzic, S. J. Yuan, L. E. DeLong, G. Murthy, and R. K. Kaul, Phys. Rev. Lett. **112**, 056402 (2014).

[22] J. H. Choy, D. K. Kim, S. H. Hwang, G. Demazeau, and D. Y. Jung, J. Am. Chem. Soc. **117**, 8557 (1995).

[23] I. Thumm, U. Treiber, and S. Kemmler-Sack, J. Solid State Chem. **35**, 156 (1980).

[24] W. T. Fu and D. J. W. IJdo, J. Alloys Compd. **394**, L5 (2005).

[25] M. Wakeshima, D. Harada, and Y. Hinatsu, J. Alloys Compd. **287**, 130 (1999).

[26] Bruker, APEX2 software suite for crystallographic programs, Bruker AXS, Inc., Madison, WI, 2009.

[27] Bruker, Area detector control and integration software, version 5.x, in SMART and SAINT, Bruker Analytical X-ray Instruments, Inc., Madison, WI, 1996.

[28] M. Sheldrick, SADABS, Program for absorption corrections, University of Goettingen, Germany, 1996.

[29] G. M. Sheldrick, Acta Crystallogr., Sect. A **64**, 112 (2008).

[30] J. Rodriguez-Carvajal, Physica B **192**, 55 (1993).

[31] For temperatures below 1.8 K only ZFC measurements have been performed.

[32] Y. Takikawa, S. Ebisu, and S. Nagata, J. Phys. Chem. Solids **71**, 1592 (2010).

[33] P. W. Selwood, *Magnetochemistry* (Interscience, New York, 1956).

[34] T. Dey, A. V. Mahajan, R. Kumar, B. Koteswararao, F. C. Chou, A. A. Omrani, and H. M. Ronnow, Phys. Rev. B **88**, 134425 (2013).

[35] P. Kayser, M. J. Martínez-Lope, J. A. Alonso, M. Retuerto, M. Croft, A. Ignatov, and M. T. Fernández-Díaz, Inorg. Chem. **52**, 11013 (2013).

[36] K. Koepernik and H. Eschrig, Phys. Rev. B **59**, 1743 (1999).

[37] URL http://www.fplo.de.